Delft University of Technology

Support Vector Machine Applied to the Optimal Design of Composite Wing Panels

dos Santos, Rogério Rodrigues; Machado, Tulio Gomes de Paula; Castro, Saullo G.P.

Important note
To cite this publication, please use the final published version (if applicable).
Please check the document version above.

Support Vector Machine Applied to the Optimal Design of Composite Wing Panels

Rogério Rodrigues dos Santos [1,*], Tulio Gomes de Paula Machado [2] and Saullo Giovani Pereira Castro [3,*]

1   Division of Mechanical Engineering, Aeronautics Institute of Technology,
    São José dos Campos 12228-900, Brazil
2   Embraer SA, São José dos Campos 12227-901, Brazil; tuliomachado10@gmail.com
3   Faculty of Aerospace Engineering, Delft University of Technology, 2629HS Delft, The Netherlands
*   Correspondence: rsantos9@gmail.com (R.R.d.S.); S.G.P.Castro@tudelft.nl (S.G.P.C.)

Abstract: One of the core technologies in lightweight structures is the optimal design of laminated composite stiffened panels. The increasing tailoring potential of new materials added to the simultaneous optimization of various design regions, leading to design spaces that are vast and non-convex. In order to find an optimal design using limited information, this paper proposes a workflow consisting of design of experiments, metamodeling and optimization phases. A machine learning strategy based on support vector machine (SVM) is used for data classification and interpolation. The combination of mass minimization and buckling evaluation under combined load is handled by a multi-objective formulation. The choice of a deterministic algorithm for the optimization cycle accelerates the convergence towards an optimal design. The analysis of the Pareto frontier illustrates the compromise between conflicting objectives. As a result, a balance is found between the exploration of new design regions and the optimal design refinement. Numerical experiments evaluating the design of a representative upper skin wing panel are used to show the viability of the proposed methodology.

1. Introduction

The development of lightweight structures is of great importance in the aeronautical and space sectors, and is progressively becoming more important in all fields of engineering due to the increasing life cycle costs related to raw materials and energy. Composite materials play an important role in lightweight design, and when compared to metallic parts, offer more design freedom. However, they require better optimization methods to find optima, and have additional challenges related to finding optimum material distributions. In the case of thin-walled laminated composite structures, finding this material distribution translates into finding the optimum number of composite layers and their respective orientations. Moreover, the design of composite panels requires finding the optimum number of stiffeners, the optimum geometry for stiffeners and the optimum laminated composite layouts that constitute the skin and stiffeners.

The use of design schemes coupling machine learning techniques with optimization algorithms is not new. Fu et al. [1] combined neural networks (NN) with genetic algorithms (GA) using mixed continuous-discrete variables, constraining the axial stiffness during the pre- and post-local buckling of the skin panels, and ultimate load. The NN was trained using the finite element method simulating at 266 sampling points. The global optimum was found using the NN coupled with the GA, and the final results were verified against the finite element model. Ehsani and Dalir [2] also proposed an NN-GA coupled approach to handle mixed continuous-discrete design variables with four continuous variables related to the width and thickness of angle-grid rib-stiffeners, and four discrete variables

related to the number and geometric orientation of those stiffening elements. The NN training took 1060 simulations using a Ritz approach. The same authors proposed pure GA optimization [3] for another gird-stiffened plate with eight continuous and three discrete design variables. In addition, 250 GA generations were used as the stopping criterion, thereby requiring thousands of evaluations to reach a converged solution.

According to the modeling and simulation perspective, an effective way to reduce the time spent on model evaluation is through the use of surrogate techniques, such as response surface and metamodeling tools. A surrogate is included in the optimization cycle in order to approximate the response of a more expensive finite element analysis. Thole and Ramu [4] proposed a modified self-organizing map algorithm to identify regions of interest (RoI) in the design space. This proposition is useful in the context of building metamodels with limited computational costs. Self-organizing maps are used as a visualization technique for design space exploration that allows the identification of regions of interest. A modified version enabled the identification of the RoI and the addition of new sampling techniques to be used within a Kriging metamodel scheme that supported the optimization cycle. Despite the clear reduction in computational load, the quality of the approximation showed to be highly dependent on the quantity and quality of the data used in the training phase, which is also valid for accelerated Kriging metamodels, recently used by Wang et al. [5,6] for finding optimal variable-stiffness layouts of composite filament-would cylinders. Therefore, for a given computational cost, a better overall optimization result is obtained when extra attention is given to the data generation process.

Branched multipoint approximate (BMA) functions proposed by Chen et al. [7] and An et al. [8] can also be used to construct approximate responses of real structures. An et al. [9] proposed the application of BMA functions on the optimization of composite laminated stiffened panels, successfully achieving optimum designs with discrete variables.

Liu et al. [10] presented a review on adaptive sampling techniques for global metamodeling, where the concept of space filling sampling was explained. The authors highlighted that classic sampling approaches have a long history in the field of design of experiments (DOE), and that their development was motivated by the design of physical experiments, and largely applied to numerical experiments. Then, the discussion of single-response adaptive sampling and multi-response adaptive sampling techniques was outlined, discussing aspects related to initial design space points, stopping criteria and trade-offs between local exploitation and global exploration. The summarized general finding is that adaptive sampling strategies provide useful feedback about the target function, and that there is not a specific strategy that always outperforms.

Support vector machine (SVM) is a classification technique belonging to the realm of machine learning. Among the desirable features are over-fitting avoidance and reduction in the amount of training data needed when compared with the neural network class of algorithms, especially for a multidimensional feature space [11]. SVM has as its main feature the ability to explicitly define complex decision functions that optimally separate two classes of data samples [12]. Thus, once the coefficient samples are categorized into two classes, SVM can provide an explicit decision function (the limit state function) separating the distinct classes. Missoum et al. [13–15] introduced the notion of an explicitly decomposed design space, whereby the limit state functions are constructed explicitly in terms of the design variables, using SVM.

In reference [15], the authors introduced an adaptive sampling scheme that reduces the number of function evaluations. The approach is based on SVM and constructs an explicit approximation of the domain boundaries with respect to the design variables. The design space is explicitly decomposed into feasible and infeasible regions. The authors handled the discontinuity of the response using a clustering technique which provides the basic classification for the construction of the SVM decision function. In a follow up study [16], the authors proposed substantial modifications by improving the choice of samples, and applying a more rigorous convergence criterion and a new technique to select the SVM kernel parameters.

Basudhar and Missoum [17] also presented a methodology for constrained global optimization, where the boundary of the feasible domain is approximated by a single SVM, and the probability of feasibility is calculated using a new probabilistic SVM model based on a sigmoid function. Two sample selection levels were used: a first stage dedicated to the global search of the constrained optimum; and a second stage focused on the local refinement of the SVM approximating the boundary of the feasible space. Their study introduced and compared an unconstrained and a constrained formulation of SVM-based optimization.

Song et al. [18] used linear and nonlinear virtual SVM in optimization problems with up to 12 variables with dynamic Kriging, finding that SVM can accurately build the decision function for the purpose of reliability-based analysis, and that SVM becomes more efficient than Kriging for high-dimensional problems.

In classification tasks, based on an independent and distributed training dataset, SVM aims at finding a discriminant function that can predict labels for new instances. From a geometric perspective, computing a classifier is equivalent to finding the equation for a multidimensional surface that best separates the different classes in the feature space. The regression problem is a generalization of the classification problem, in which the model provides a continuous-valued output.

The present paper proposes a new methodology to obtain optimal designs of composite stiffened panels. The panel consists of a representative segment of a wing's upper skin, whereby the local loads are calculated considering the global wing behavior. The design parameterization considers the number of stiffeners, the geometry of the stiffeners and the composite layup for the stiffeners and the skin. During the optimization, the number of high fidelity samples to be evaluated is guided by a design of experiment (DOE) based on the Latin hypercube algorithm [19]. The DOE data supports a SVM model that is able to classify between feasible and infeasible designs.

The main scientific contributions of the paper are:

- Use a limited and pre-determined number of high-fidelity finite element evaluations based on the DOE requirements;
- Use multiple objectives of continuous optimization (in opposition to integer optimization), whereby interpolation and classification objectives are built utilizing SVM models;
- Generate a Pareto frontier that discusses the contributions of mass and feasibility (buckling constraint) to the optimal design.

The paper is organized as follows. Section 2 presents the wing model, load idealization and buckling analysis. The methodology is presented in Section 3, addressing design parameterization, optimization workflow and data analysis. Section 4 shows the numerical results. Conclusions are presented in Section 5.

2. Structural Modeling

In the present study, only a single up-bending load case was considered, and it was assumed that the distributed load over the wing could be in equilibrium with a bending moment (BMX) and a transverse shear load (SLZ) at the wing root, as illustrated in Figure 1. These design loads were determined by assuming the wing to be a cantilever beam and subjected to an idealized elliptical lifting load distribution along the half span. The resultant load was derived considering the aircraft maximum take-off weight and maximum flight load factors, resulting in BMX = 215 kNm and SLZ = 80 kN for the current study case. Note that the contributions from the wing weight on the bending, the torsion moments and the in-plane bending moment caused mainly by drag forces were ignored.

In order to evaluate the structural response at the wing root, a finite element (FE) model was constructed based on a representative cell of a double half-bay model, as proposed by Fenner [20], which is a stringer-skin assembly consisting of two halves of adjacent wing bays separated by a middle rib, where the nodes have zero normal displacements. Note that any cross-section other than the wing root could have been selected, and the present

study focused on the wing root. The representative cell is a fraction of the entire panel and includes one longitudinal stiffener segment attached to the skin. The skin width was equal to the spacing between adjacent stiffener segments. The length of the representative cell extended longitudinally from one adjacent mid-bay to the other, as delimited by the red box region shown in Figure 2. The representative cell approach is convenient during a preliminary design phase where only few design characteristics are completely defined and frequent design modifications require a rapid tool for concept validation. Machado et al. [21] coupled this modeling scheme for the optimization of stiffened panels using genetic algorithms.
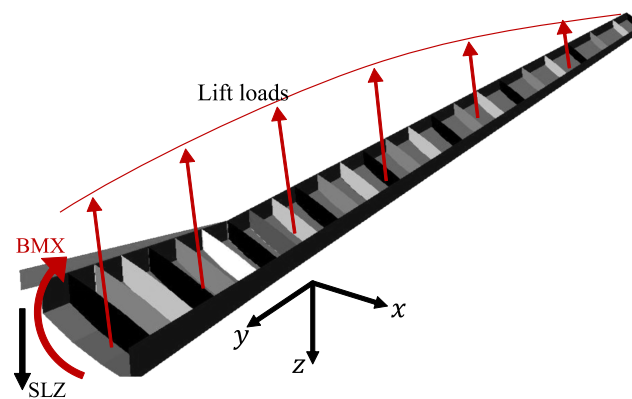
Figure 1. Wing model, coordinate system and idealized loads at the wing root. SLZ: shear load in the *z* direction. BMX: bending moment about the *x* direction.
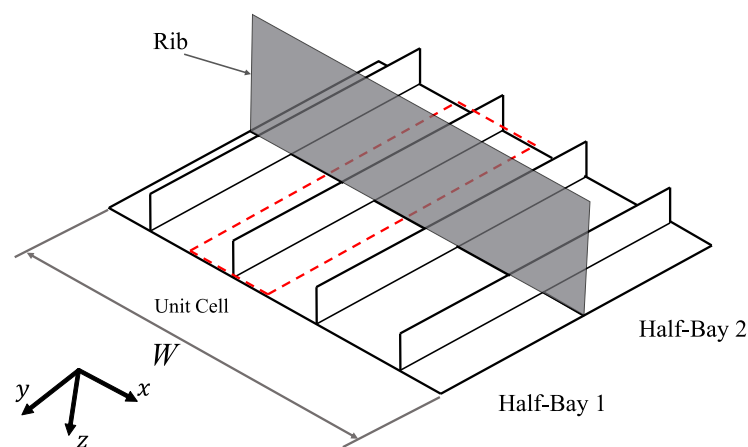

Figure 2. Schematic definition of the representative unit cell of the stiffened panel, depicted by the red dashed line. The width of the panel bay *W* is a given geometric parameter.

The FE model of the representative cell is based on general-purpose quadrilateral plate elements with bi-linear displacement interpolation within the element domain. In Nastran, these elements are known as CQUAD4 [22], having four nodes and six degrees-of-freedom per node, being the translations parallel to x, y, z, and the three respective rotations about these three axes. The symmetric boundary condition is used in the four edges, as depicted in Figure 3. The edges perpendicular to the chord-wise direction are constrained in translation along the y direction and rotations with respect to the x and z-axes. The edges perpendicular to the span-wise direction are constrained in rotation with respect to the y and z-axes. Moreover, nodal translations are constrained at the bottom edge in x direction, and the rib placed in the middle of the representative cell creates a support in the z direction, such that the corresponding nodes are constrained for normal translations.

The longitudinal stringer is composed of a pair of L-shaped stringers joined in their shared mid-plane to form a T-shape or blade-type stringer, making the laminate at the stringer web symmetric over the mid-plane. Hence, the laminate at the stringer foot is

allowed to be asymmetric. With the default setting, MSC Nastran® [22] calculates the thickness of the plate element with respect to the reference plane determined by the nodes within the element, creating a symmetrical thickness distribution profile shown in the laminate cross-section. However, the symmetric thickness distribution about the mid-plane is not consistent with the manufacturing of these panels. Thus, in order for the FE model of Figure 3 to correctly represent the as-manufactured cross-section of Figure 4, the shell elements representing the skin and stiffener's base regions must be offset from the reference plane by a value $t_{sk}/2 + t_{str}/4$, with t_{sk} and t_{str} being the local skin and stiffener's thicknesses. Note that the thickness of the stiffener's base laminate, i.e., the region connected to the skin, is $t_{str}/2$.
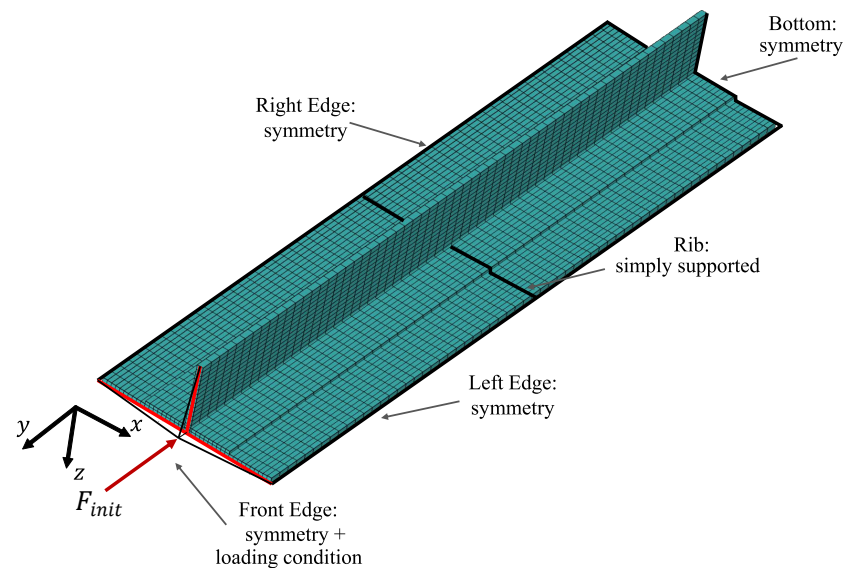
Figure 3. Double half-bay symmetric FE model for the representative unit cell. Force F_{unit} represents the unitary compressive load applied for the first linear buckling analysis.
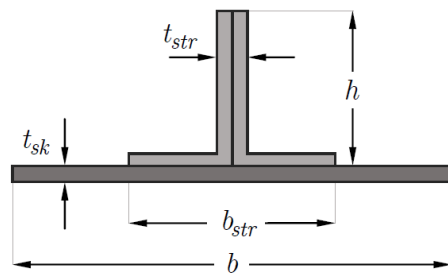
Figure 4. Cross-section of the blade-type stiffened panel representative cell.

The properties for carbon-epoxy unidirectional plies used in the present study are extracted from Kassapoglou [23] E_1 = 137.88 GPa, E_2 = 11.72 GPa, v_{12} = 0.3, G_{12}= 4.825 GPa, ρ = 1600 kg/m^3 and t_{ply} = 0.1524 mm.

2.1. Load Idealization

In a preliminary design, it is desirable to have a rapid and accurate method to calculate loads for a representative cell of the panel. A structural idealization of the wing root cross-section was employed according to Megson [24], where the longitudinal stiffeners were treated as concentrated areas carrying only axial stresses, whereas the idealized skin carried the shear stresses. The bending stresses were determined by:

$$\sigma_y = \left(\frac{M_z I_{xx} - M_x I_{xz}}{I_{xx} I_{zz} - I_{xz}^2} \right) x \; + \; \left(\frac{-M_x I_{zz} - M_z I_{xz}}{I_{xx} I_{zz} - I_{xz}^2} \right) z \tag{1}$$

where M_x = BMX of Figure 5; $Mz = 0$ in the present work; I_{xx}, I_{zz}, I_{xz} are second moments of area calculated using the idealized cross-section. The design loads BMX = 215 kNm and SLZ = 80 kN previously mentioned were used in the wing bay optimization process. The shear flow distribution over the idealized wing section q_s was determined by Equation (2)

$$q_s = q_b + q_{s,0} \tag{2}$$

where q_b is the shear flow induced in an equivalent virtually opened section and $q_{s,0}$ a correction shear flow. For any given section, q_b was calculated by virtually crating a cut that opened the closed section, and using the concentrated areas B_r with their respective positions in the idealized section, as per Equation (3):

$$q_b = - \left(\frac{S_x I_{xx} - S_z I_{xz}}{I_{xx} I_{zz} - I_{xz}^2} \right) \sum_{r=1}^{n} B_r x_r \; - \; \left(\frac{S_z I_{zz} - S_x I_{xz}}{I_{xx} I_{zz} - I_{xz}^2} \right) \sum_{r=1}^{n} B_r z_r \tag{3}$$

The term $q_{s,0}$ in Equation (2) is determined from the equilibrium of moments given in Equation (4)

$$S_x \eta_0 - S_z \epsilon_0 = \oint q_b p \, ds + 2A \, q_{s,0} \tag{4}$$

where the equilibrium is taken from an arbitrary axis. The left-hand side represents the moment of the external shear forces S_x and S_z, which are offset from the moment axis by η_0 and ϵ_0, measured, respectively, in the z and x axes. The closed integral on the right-hand side represents the moments generated by the shear flow distribution q_b, calculated per Equation (3); and the area A corresponds to the area enclosed by the idealized section.
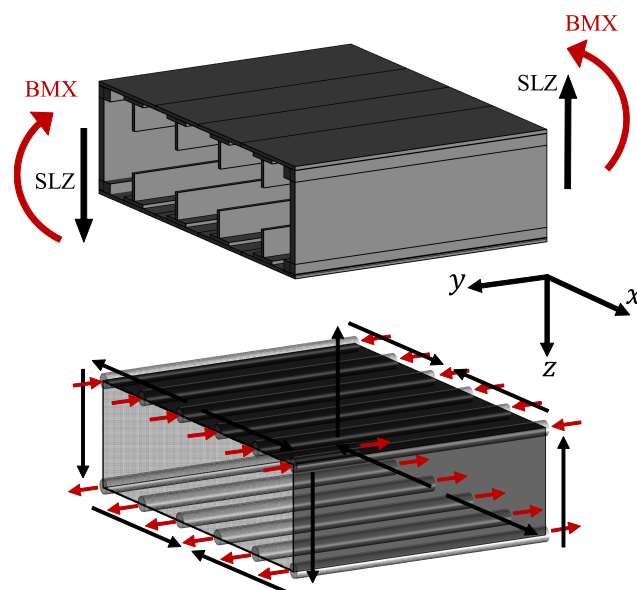
Figure 5. Load idealization. Top: bending moment (BMX) and shear force (SLZ) equilibrium on a single bay. Bottom: modified boom method to obtain the distributed loads of each representative cell.

The idealized cross-section discretization and calculation of local axial and shear stresses are particularly interesting in the present study, as the actual wing bay section

had to be discretized into booms to determine stress acting on the skin, based on the geometrical parameters from the skin and stiffener. In the optimization problem, the design variables within each individual evaluated by the genetic algorithm define a unique skin-stringer assembly, with a given geometry and skin and stringer thicknesses that automatically determines the configuration of the booms, but also determines the most stressed skin-stringer assembly within a wing bay. The peak stress in the upper skin panel was used to define the compression state for the entire upper panel by simply multiplying the acting stress by the skin-stringer assembly cross-sectional area. With this approach, each individual stiffener, with the adjacent skin pockets, carries the correct load with consistent compressive stresses generated thereof, all as a function of the optimization design variables.

2.2. Buckling Analysis

Combined shear and compression buckling will be used to evaluate the wing panels. This is implemented in MSC Nastran by means of two linear buckling analyses performed on each evaluated individual along the optimization. MSC Nastran's SOL 105 Lanczos Eigensolver is used to obtain the critical buckling loads. **The first linear buckling analysis** aims at determining the critical compressive force of the panel F_{cr}, with the pre-buckling state created using a unitary force $F_{unit} = 1\ N$ distributed in the front edge by means of a rigid element with a single master node, as illustrated in Figure 3. The critical load is calculated with $F_{cr} = \lambda_1 F_{unit}$, where λ_1 is the first eigenvalue of the first analysis. **The second linear buckling analysis** evaluates the critical in-plane shear distributed force, or shear flow, of the panel q_{cr}, with the pre-buckling state created assuming a unitary in-plane shear flow $q_{unit} = 1\ N/m$. This unitary shear force is translated into nodal forces and distributed over the FE model, as illustrated in Figure 6, with the nodal forces calculated using the lengths of the representative cell in x and y directions, given by ℓ_x, ℓ_y, and the number of nodes along the edges in each direction, $N_{nodes\,x}, N_{nodes\,y}$, as per Equation (5). The critical shear force is calculated with $q_{cr} = \lambda_2 q_{unit}$, where λ_2 is the first eigenvalue of the second linear buckling analysis.

$$F_{shear\,x} = \frac{q_{unit}\ \ell_x}{N_{nodes\,x} - 1}$$

$$F_{shear\,y} = \frac{q_{unit}\ \ell_y}{N_{nodes\,y} - 1}$$

(5)
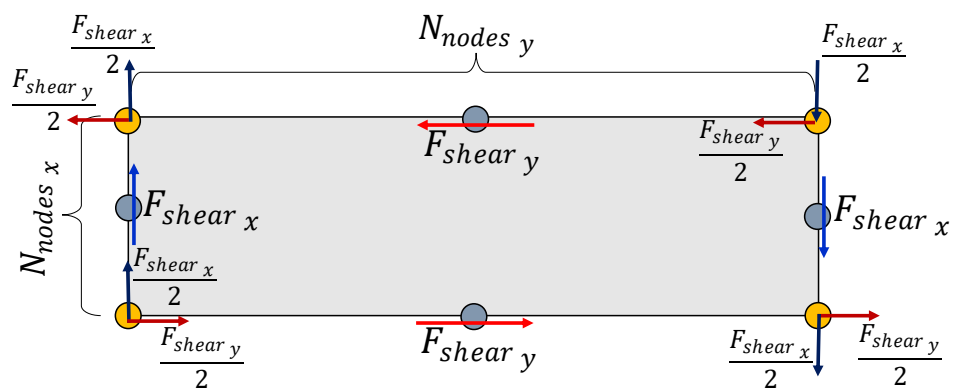
Figure 6. Detailed representation of the distribution of shear loads on the representative cell.

The design constraint is the margin of safety for combined shear and compression buckling. The interaction curve suggested by Kassapoglou [23] was adopted, as given in Equation (6), coupling the compression and shear effects. In this formulation, σ_y and τ_{xy} correspond to the current compression and shear stresses, whereas σ_{cr} and τ_{cr} are the critical buckling stresses for compression and shear. With the combined stress state, the panel buckles when the inequality presented in Equation (6) is not satisfied.

$$\frac{\sigma_y}{\sigma_{cr}} + \left(\frac{\tau_{xy}}{\tau_{cr}}\right)^2 \leq 1 \tag{6}$$

In the FE model the pre-buckling state is created by means of applied forces, and hence it is convenient to rewrite Equation (6) in terms of the acting compression force $F_y = \sigma_y A$ and the shear flow $q_s = \tau_{xy}/t_{sk}$, where A is the cross-sectional area of the skin-stringer assembly and t_{sk} is the skin thickness. Hence, the failure index for combined buckling of one representative cell FI_{cell} is:

$$FI_{cell} = \frac{F_y}{F_{cr}} + \left(\frac{q_s}{q_{cr}}\right)^2 \tag{7}$$

and to prevent failure, FI_{cell} must be constrained such as:

$$FI_{cell} \leq 1 \tag{8}$$

The acting force F_y is determined with the actual compressive stress due to bending σ_y, calculated for the entire cross-section using Equation (1) for a idealized wing box section, as illustrated in Figure 7a. Similarly, the shear flow q_s over the wing box section is calculated using Equation (2), as illustrated in Figure 7b. In order to determine the most stressed representative cell, the interaction curve equation is evaluated for all possible combinations of the ith stringer in the panel with the adjacent jth skin pocket. Conservatively, the stiffened panel bay is sized based on the most critical representative cell within the entire bay. The critical failure index for combined buckling, I_{cr}, is calculated considering the FI_{cell} calculated for every cell, such that:
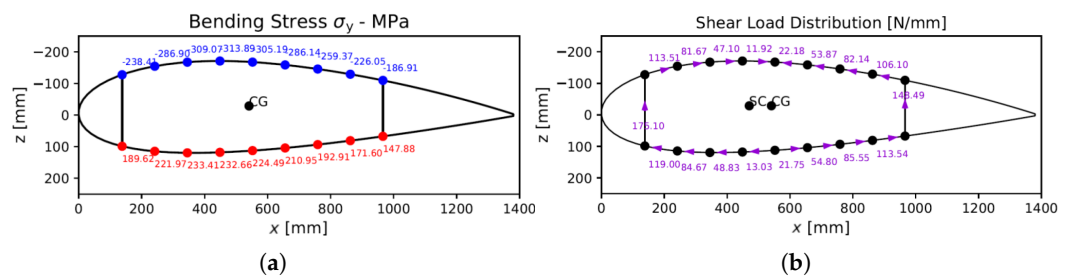
$$FI_{cr} = \max(FI_{cell}) \tag{9}$$

Figure 7. (**a**) Axial stress distribution due to bending loads; and (**b**) shear flow distribution due to shear loads.

3. Methodology for the Design and Optimization

3.1. Design Parameterization

The parameters controlling the design are separated into geometric and stiffness variables. The geometric variables are shown in Figure 4: t_{str} and h, the thickness and height of the stiffener's web, respectively; b_{str}, the width of the stiffener's base; and t_{sk} and b, the thickness and width of the skin segment, respectively. Note that the longitudinal length of the representative cell was assumed to be constant and equal to 800 mm.

The design variables and respective SI units are:

1. Width of the representative cell [m]: b;
2. Stringer height [m]: h;
3. Stringer base width [m]: b_{str};
4. Number of skin plies at 0°: $n_{0°}^{sk}$;
5. Number of skin plies at 45°: $n_{\pm45°}^{sk}$;
6. Number of skin plies at 90°: $n_{90°}^{sk}$;
7. Number of stringer plies at 0°: $n_{0°}^{str}$;
8. Number of stringer plies at 45°: $n_{\pm45°}^{str}$;

9. Number of stringer plies at 90°: $n_{90°}^{str}$,

grouped in vector:

$$\boldsymbol{x} = [b, h, b_{str}, n_{0°}^{sk}, n_{\pm45°}^{sk}, n_{90°}^{sk}, n_{0°}^{str}, n_{\pm45°}^{str}, n_{90°}^{str}]^T. \tag{10}$$

The width of the skin segment b is the representative cell width, or the stringer spacing, directly related to the number of stringers in the whole bay panel. In the proposed optimization scheme, the acting force of Figure 3, F, is a function of the design variables $\boldsymbol{x}$, and consistently calculated for each individual configuration of the stiffened panel representative cell for a given stringer spacing, stringer height and thickness distribution.

Table 1 gives the discrete values for all optimization variables. The discrete values for the stringer spacing b are obtained assuming that a minimum of 5 and maximum of 8 stringers can be used. For b_{str}, the minimum dimension is determined based on minimum fastener spacing guidelines [25]; and for h the range is chosen based on arbitrary values that render profiles of proportional dimensions. The variables defining the composite laminates are given by the numbers of unidirectional plies oriented at 0°, ±45° and 90° for the skin and stringer, named, respectively, $n_{0°}^{sk}, n_{\pm45°}^{sk}, n_{90°}^{sk}$ and $n_{0°}^{str}, n_{\pm45°}^{str}, n_{90°}^{str}$. Assuming a laminate ply thickness of $t_{ply} = 0.1524$ mm, the skin thicknesses is calculated using $t_{sk} = t_{ply}\left(n_{0°}^{sk} + n_{\pm45°}^{sk} + n_{90°}^{sk}\right)$, and the stringer web thickness using $t_{str} = 2\,t_{ply}\left(n_{0°}^{str} + n_{\pm45°}^{str} + n_{90°}^{str}\right)$. Note that at least one layer in each orientation is required, and for ±45° the layers are changed in pairs to keep the designed laminates balanced. The stacking sequence is ignored in the present approach, meaning that the composite mechanical representation ignores the terms related to shear-extension coupling, bending-twist coupling and bending-extension coupling [26].

Table 1. Design variables and discrete values.

Design Variable	Discrete Values
b	105, 120, 140, 168 mm
h	40, 50, 60, 70, 80 mm
b_{str}	30, 40, 50, 60, 70 mm
$n_{0°}^{sk}$	$1, 2, \cdots, 10$
$n_{\pm45°}^{sk}$	$2, 4, \cdots, 20$
$n_{90°}^{sk}$	$1, 2, \cdots, 10$
$n_{0°}^{str}$	$1, 2, \cdots, 10$
$n_{\pm45°}^{str}$	$2, 4, \cdots, 20$
$n_{90°}^{str}$	$1, 2, \cdots, 10$

3.2. Optimization Pipeline

The computational model previously described was used to evaluate the stability behavior by means of the combined margin of safety for buckling, presented in Equation (7). With no further information about the problem under consideration, evolutionary methods such as genetic algorithms or simulated annealing are alternatives that have an effective strategy for enumerating good designs. However, these approaches require a large number of objective evaluations, especially the genetic algorithms [21].

In our analysis of mixed continuous-discrete variables, the authors noted a high sensitivity of the linear buckling eigenvalue with the design variables. The optimization process uses a nonlinear programming algorithm and continuous design variables. The optimal design is rounded off to the nearest integer. Furthermore, aiming at reducing the estimate error, an SVM model is used to classify a new design value as feasible or infeasible according to Equation (7).

Motivated by the possibility to reduce the number of FE evaluations while still obtaining the design region of global optimality, the present study proposes a new strategy for the design enumeration, evaluation and optimization. It is hypothesized that only a pre-

determined and fixed number of $m + n$ FE evaluations is required, where m is the number of initial design samples, and n is the number of optimization problems generated. The workflow of the proposed design framework, illustrated in Figure 8, can be summarized as follows:

1. Generate the design of experiments (DOE) $\pmb{x_0} \in \mathbb{R}^{m \times 9}$ for the design variables;
2. Compute the failure index as per Equation (7) for each of the m FE models in the $\pmb{x_0}$ designs;
3. Compute the mass index, feasibility index and feasibility classification at $\pmb{x_0}$, as described next;
4. Find the optimal design $\pmb{x_1}$ by the optimization of the objective (step 3) starting at $\pmb{x_0}$;
5. Evaluate the FE model at the n optimal designs $\pmb{x_1}$;
6. Compute the mass of the structure at the feasible designs points;
7. If new investigation is required, add information generated by $\pmb{x_1}$ designs in step 5 to the initial set $\pmb{x_0}$ and go to step 3; otherwise, stop.

Step 7 consists of a feedback trigger that guides to the evaluation of new design points, usually conducted if further investigation of the transition between feasible and infeasible designs is desired. In this case, a new DOE will be established in the vicinity of the current optimal design. Thus, the final step can be understood as a trigger for restarting the process, in which case a new analysis will be carried out taking into account all the knowledge generated so far. In case the analysis is carried out only to evaluate the compromise between mass and feasibility, step 7 of the workflow mentioned above is not necessary.

Considering the vector with all design variables $\pmb{x}$ given in Equation (10), there are lower $\pmb{x_l}$ and upper $\pmb{x_u}$ bounds for the design variables, defined as:

$$\pmb{x_l} = [105, 40, 30, 1, 2, 1, 1, 2, 1]^T \tag{11}$$

and

$$\pmb{x_u} = [168, 80, 70, 10, 20, 10, 10, 20, 10]^T \tag{12}$$

Furthermore, a mass index, feasibility index and feasibility classification are computed for each design $\pmb{x}$ using the FE model data. The mass index is defined as:

$$O_1(\pmb{x}) \in \mathbb{R}^+ \tag{13}$$

and the feasibility index is:

$$O_2(\pmb{x}) \in \mathbb{R}^+ \tag{14}$$

For the case $O_2(\pmb{x}) \leq 1$, the design is feasible, and for $O_2(\pmb{x}) > 1$, it is infeasible. Thus, the feasibility classification index can be written as:

$$O_3(\pmb{x}) \in \{0, 1\} \tag{15}$$

with the design being feasible when $O_3(\pmb{x}) = 0$, and infeasible when $O_3(\pmb{x}) = 1$. Those indices are used to build the objective function, as discussed in the next sections.
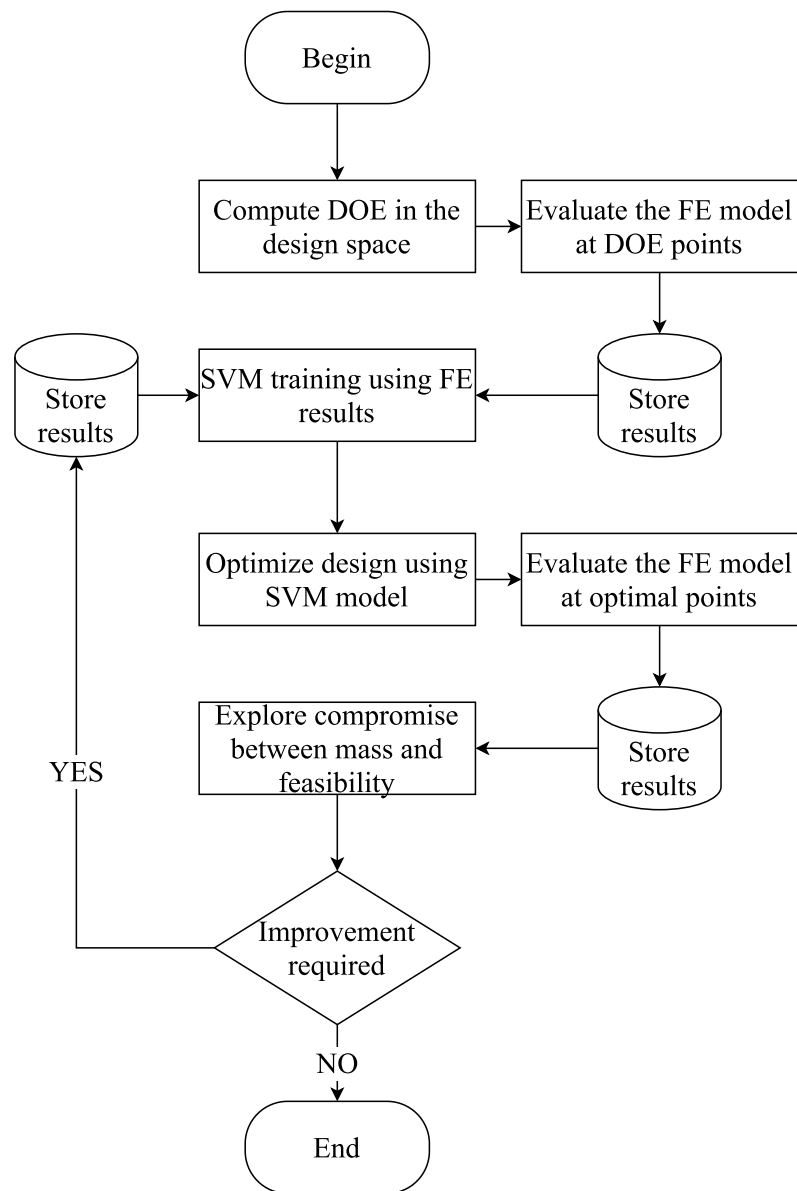
Figure 8. Optimization workflow.

The Latin hypercube sampling (LHS) method [19] was used to establish the s_i sample points, $i = 1, \ldots, 1000$. The FE model was then evaluated for those s_i designs. Mass and feasibility values obtained from this evaluation are represented in Figure 9. A feasibility value greater than 1 indicates that the structure failed in operation. Therefore, the corresponding design is infeasible from the mechanical perspective. According to Figure 9, 35% of the designs provided by the DOE led to infeasible configurations.
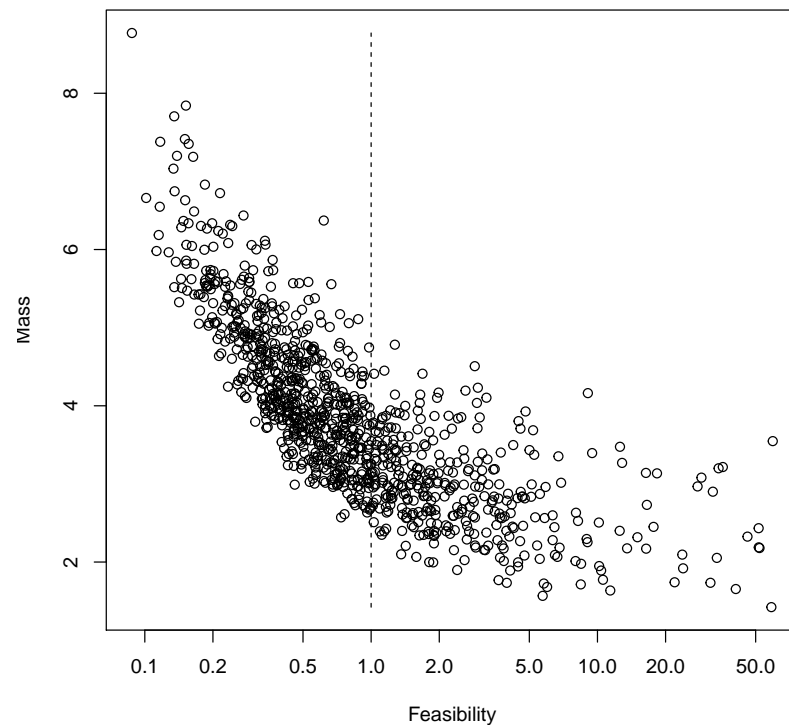
Figure 9. Mass and feasibility indices for the first DOE.

3.3. SVM Formulation

An interesting characteristic of machine learning algorithms is their ability to generalize the training experience and provide an unexpected output that best fulfills the objective function, thereby predicting future events or scenarios that are not explicitly mapped in the training process. They can therefore reach results that are unexpected and non-intuitive. Among a myriad of alternatives for implementing a learning strategy, a comprehensive overview of popular strategies and resources was presented in [27].

The standard SVM is formulated as a classifier whose decision function is represented by a hyperplane that maximizes the distances of separated samples from different classes. Using the hyperplane, the unknown outputs are estimated by an appropriate interpolation of the evaluated designs, according to the DOE used for training. Therefore, a limited number of m FE evaluations is pre-determined and fixed before the optimization. The exploration of the design space is conducted by the optimization algorithm using the hyperplane approximation, which implies a significant reduction of the computational cost required to evaluate the design space during the optimization. Once the optimal design is obtained, the mass and feasibility indices are updated by using the FE model. Given a labeled training dataset $\{x_i, y_i\}$, where $x_i \in \mathbb{R}^N$ and $y_i \in \{-1, 1\}$, and a nonlinear mapping $\phi(\cdot)$, the method solves:

$$\min_{w, \xi, b} \left(0.5 \parallel w \parallel^2 + C \sum_{i=1}^{n} \xi_i \right) \tag{16}$$

subject to:

$$y_i(\langle \phi(x_i), w \rangle + b) \geq 1 - \xi_i, \ \forall i = 1, \ldots m \tag{17}$$

where:

$$\xi_i \geq 0, \ \forall i = 1, \ldots m \tag{18}$$

with w and b defining a linear classifier in $\mathbb{R}^N$. In the present study, $N = 9$ was the number of design variables and $m = 1000$ was the number of design samples. Equation (16) minimizes the norm of the model weights and the committed errors. An appropriate choice of the nonlinear mapping leads to transformed samples that are more likely to be linearly

separable in the higher dimensional feature space. The regularization parameter C controls the generalization capability of the classifier.

The methodology ultimately finds a linear combination of features that characterizes or separates two or more classes of objects or events (as described by y_i). Since the convex optimization problem is solved by a deterministic algorithm, for a specific input dataset the same optimal hyperplane parameter is obtained, as a solution of Equations (16)–(18). The SVM method automatically determines the model complexity by selecting the number of support vectors, as expressed by the parameter C in Equation (16). A detailed discussion about the SVM method and variants can be found in Awad and Khanna [11] and Salcedo-Sanz and Rojo-Álvarez [28].

4. Numerical Results

4.1. Metamodel Comparison

An investigation was conducted to compare the performance of the SVM algorithm with those of neural network architectures. SVMs and neural networks each consist of a set of methodologies, and several implementations are available in each category. The present study used the SVM implementation provided by the liquidSVM library [29]. The multi-layer perceptron neural network (MLPNN) [30] and radial basis function neural network (RBFNN) [31] were used via the Stuttgart Neural Network Simulator [32].

A set of $m = 1000$ sample points was randomly divided into two groups. The training set consisted of 700 points, and the testing set contained 300 observations. The metamodel was calibrated using the training set. Then the error was computed by using the information of the testing set.

Table 2 shows the metamodel error in mass estimation. The table columns display the following statistics: minimum, first quantile, median, mean, third quantile and maximum error values. The mean error of the SVM was 2.18×10^{-2}. The mean error of RBFNN was 0.21. The mean error of MLPNN was 0.65. The dispersion of the data followed a similar trend. SVM showed the best performance.

Table 2. Metamodeling error in mass computation.

Metamodel	Min.	1st Qu.	Median	Mean	3rd Qu.	Max.
SVM	1.004×10^{-5}	7.243×10^{-3}	1.487×10^{-2}	2.187×10^{-2}	3.152×10^{-2}	1.717×10^{-1}
RBFNN	0.00032	0.06771	0.14846	0.21802	0.28282	1.94824
MLPNN	0.06726	0.59707	0.67307	0.65497	0.72852	0.86448

Table 3 shows the metamodel error in the feasibility estimate. The average error of the SVM metamodel was 2.00, that of RBFNN metamodel was 2.05 and that of MLPNN was 2.09. There are small differences among the errors of the metamodels, although SVM performed slightly better. The relatively high error levels confirm the fact that estimating the feasibility index is a challenging task.

Table 3. Metamodeling error in feasibility index computation.

Metamodel	Min.	1st Qu.	Median	Mean	3rd Qu.	Max.
SVM	0.00054	0.65989	1.58148	2.00729	2.87262	11.59350
RBFNN	0.00025	0.46714	1.10598	2.05893	2.72801	24.07796
MLPNN	0.00380	0.44705	1.11403	2.09116	2.75163	24.93674

In the present case, the neural network models used `size = 300` as the number of units in the hidden layers and `maxit = 1000` as the maximum iterations to be learned. On the other hand, SVM used the parameters `max_gamma = 3125` and `min_lambda = 2.4 × 10`$^{-9}$. All three methodologies support the selection of different kernel methods, and a myriad of parameter combinations. As a result, the comparison of metamodels can lead to different results if fine-tuning is performed for each methodology.

Due to the good results provided by the SVM methodology in the default configuration, it was used in the analysis that follows.

4.2. Data Analysis

The arrangement of SVM models as performance indices is detailed in the following. Three SVM models are proposed. The first model, named f_1, computes a mapping of the design vector $\boldsymbol{x}$ (Equation (10)), the input data, to the mass of the structure $O_1(\boldsymbol{x})$ (Equation (13)), the output data. The second model, f_2, computes a mapping of the design variables (input data) to the feasibility index O_2 (Equation (14)), the output data. The third model, f_3, performs a binary classification task, mapping the design variables (input data) to a feasibility classification O_3 (Equation (15), 0 for feasible designs and 1 for infeasible designs). The *liquidSVM* library [29] was used for numerical computation, as provided by the R software [33]. In summary:

$$f_1 \text{ is the metamodel of mass index } f_1 : \boldsymbol{x} \rightarrow O_1, \tag{19}$$

$$f_2 \text{ is the metamodel of feasibility index } f_2 : \boldsymbol{x} \rightarrow O_2, \tag{20}$$

and

$$f_3 \text{ is the metamodel of feasibility classification } f_3 : \boldsymbol{x} \rightarrow O_3. \tag{21}$$

A comparison between the mass values obtained through FE evaluation and the estimates provide by the metamodel is presented in Figure 10.
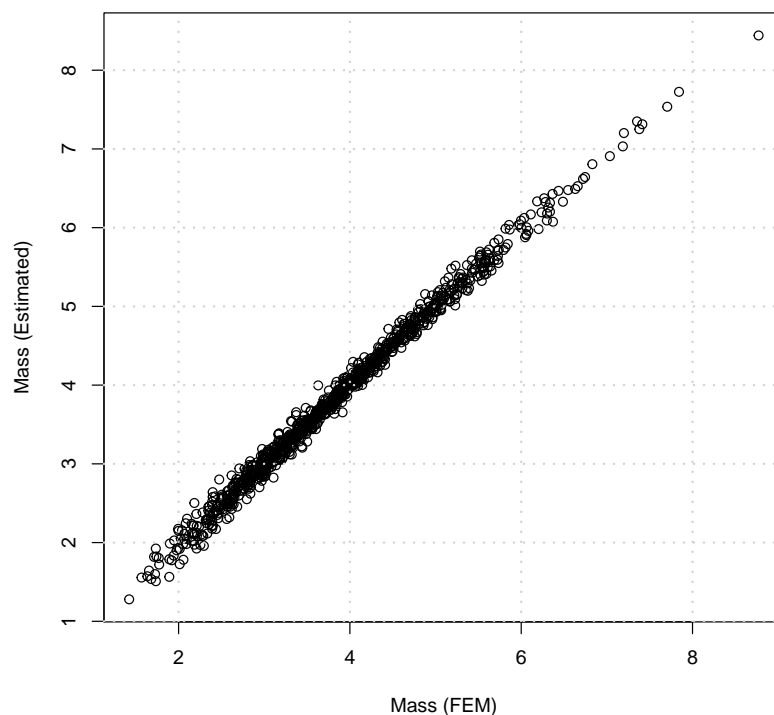

Figure 10. Mass values computed by FE and the metamodel.

The absolute value of the difference between the mass computed by FE and the estimate is

$$\Delta_1(\boldsymbol{x}) = |O_1(\boldsymbol{x}) - f_1(\boldsymbol{x})| \tag{22}$$

and a comparison of error against mass is shown in Figure 11. An histogram of the error Δ_1 representing the difference between the mass computed by the FE model and the mass estimated by Equation (13) is computed using Equation (22), and shown in Figure 12.

The results obtained from the FE and the estimates of the metamodel are similar, and the mass value was estimated with accuracy, as shown in Figure 10. Figure 13 shows

a comparison between the feasibility values obtained through FE evaluations and the estimate provided by the metamodel.

The difference between the feasibility index computed by FE and the estimate is

$$\Delta_2(\boldsymbol{x}) = |O_2(\boldsymbol{x}) - f_2(\boldsymbol{x})| \tag{23}$$

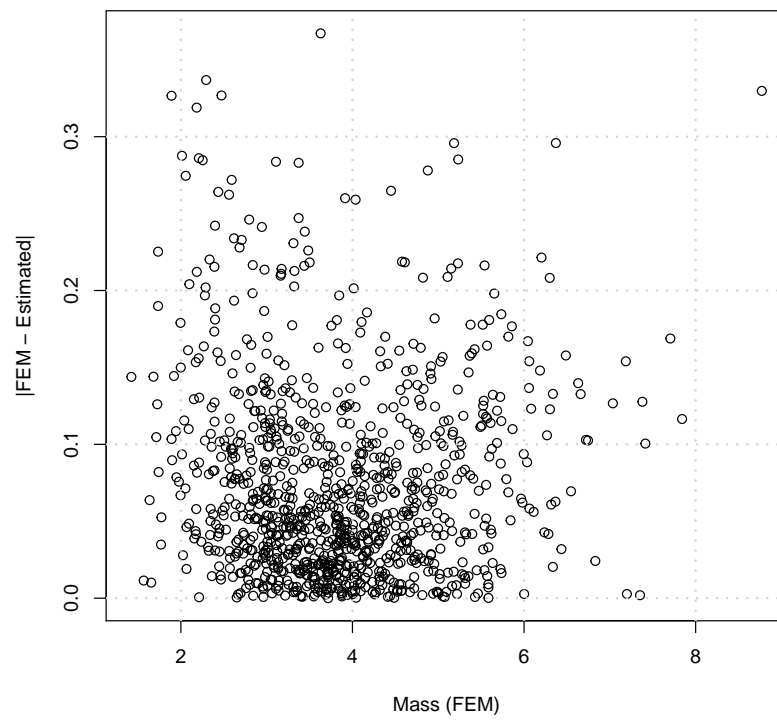whose absolute value is plotted against feasibility, as shown in Figure 14.

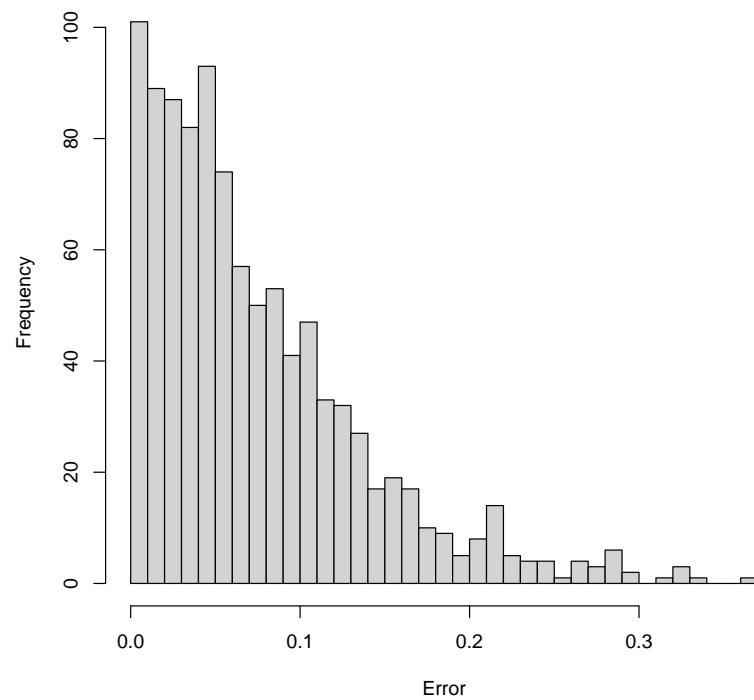**Figure 11.** Mass values computed by FE and the metamodel.

Figure 12. Histogram of the error Δ_1.

The histogram of the error Δ_2, as per Equation (23), is presented in Figure 15.

Figure 13 shows that there is no clear trend between the design variables and the feasibility index; that is, some estimates are not representing the value obtained from FE with accuracy. This training phase required 1 second to calibrate the mass estimate and 218 s for the feasibility index. Given the poor correlation with the feasibility index, a more robust method is needed to classify the feasibility of the stiffened panel designs. A new feasibility classification is proposed to improve the success rate in obtaining optimal feasible designs. The step function ($f_3(\boldsymbol{x}) = 0$ for feasible designs and $f_3(\boldsymbol{x}) = 1$ for infeasible designs) was an effective improvement for the optimization formulation. The preference of mass or feasibility improvement is addressed by the parameter $\alpha \in [0.05, 0.95]$. The multi-objective optimization formulation is written as

$$F(\boldsymbol{x}) = \left(\alpha \cdot f_1(\boldsymbol{x})^2 \right) + [(1 - \alpha) \cdot (f_2(\boldsymbol{x}) + f_3(\boldsymbol{x}))]. \tag{24}$$
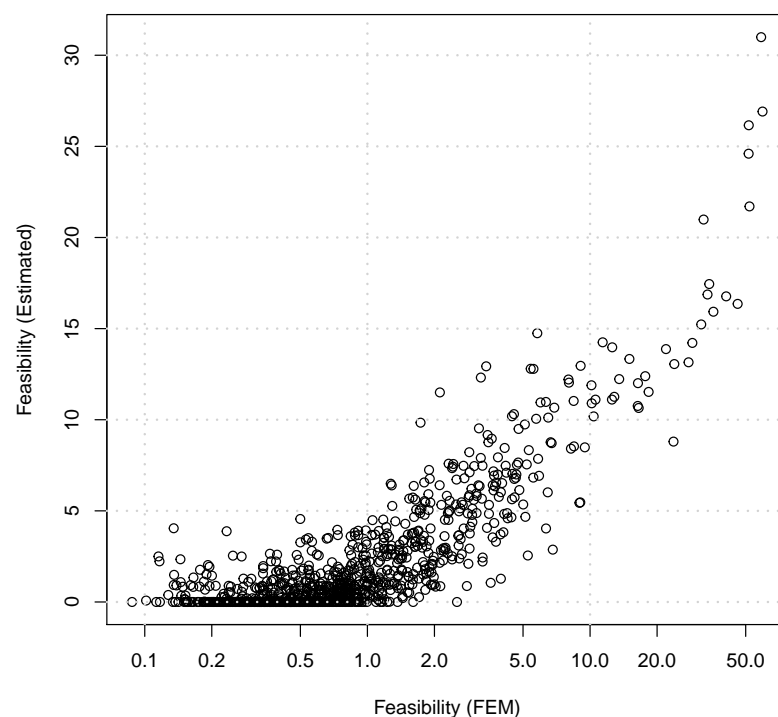

Figure 13. Feasibility index values computed by FE and the metamodel.

The design variables are box constrained (Equations (11) and (12)) by

$$\boldsymbol{x_l} \leq \boldsymbol{x} \leq \boldsymbol{x_u}. \tag{25}$$

Due to the discontinuous nature of the problem created mainly by the layout design variable b, the computation of gradients is difficult, and the authors aimed to avoid gradient evaluations using finite differences. The aforementioned discontinuity leads to non-smooth behavior that fits better to an optimization method that does not require explicit gradient evaluations. It is estimated by a quadratic approximation on the BOBYQA algorithm [34], which is adequate for the bound-constrained minimization in the absence of gradient information, and was used as implemented in the NLopt library [35].

A discussion about the error between estimated and FE values follows. Figure 16 shows the mass against the feasibility index. Those values were obtained from DOE designs. The abscissa has valued of $log(O_2(\boldsymbol{x}))$ and the ordinate represents the mass index $O_1(\boldsymbol{x})$. The color palette represents the Δ_1 error level. Designs with a small error are plotted in green, whereas designs with large errors are plotted in red. Larger errors were found in the range of infeasible designs $O_2(\boldsymbol{x}) > 1$ and in the range of high mass values $O_1(\boldsymbol{x}) > 5$ kg.
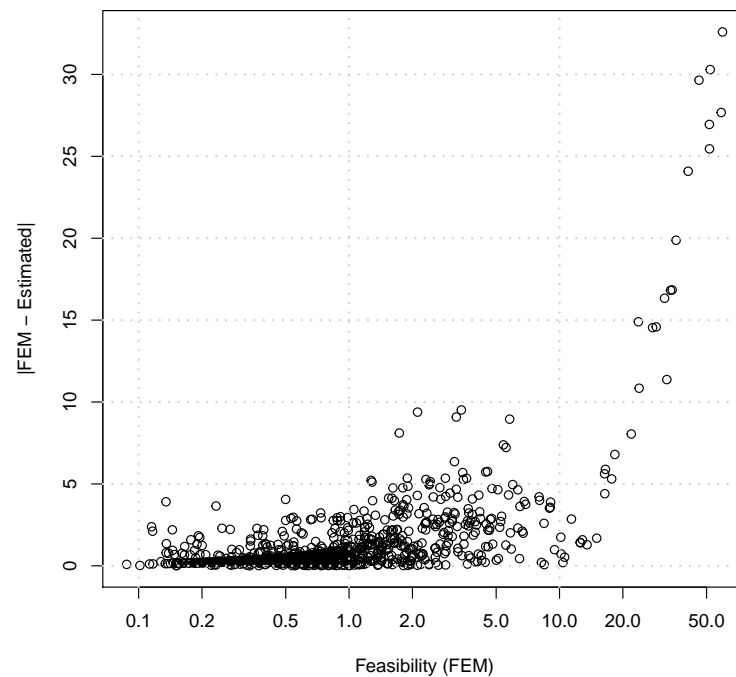
Figure 14. Feasibility index values computed by FE and the metamodel.
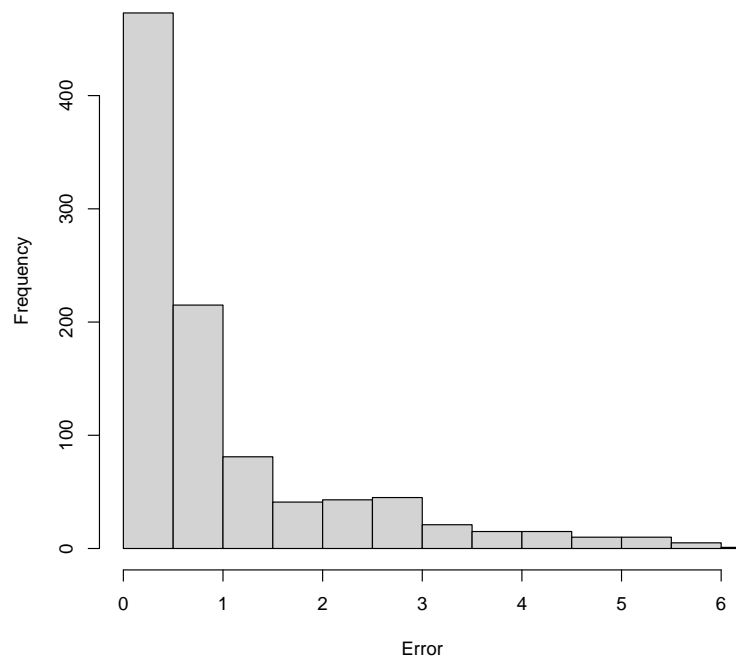
Figure 15. Histogram of the error Δ_2.

Figure 17 shows the error of the feasibility index. The abscissa has values of $log(O_2(\boldsymbol{x}))$, and the ordinate represents the mass index $O_1(\boldsymbol{x})$. The error $log(\Delta_2)$ is in green for small values and red for large values. Larger errors were found in the range of infeasible designs $log(O_2(\boldsymbol{x})) > 0$, that is, where $O_2(\boldsymbol{x}) > 1$.

The presence of an SVM-based classification index in the objective function enabled a deterministic optimization method to obtain the optimal design, yet with the ability to provide insight about the improvement obtained when mass and feasibility have different priorities, controlled by the weighting parameter α. The change in priority of mass value against feasibility leads to distinct optimal designs, addressing the compromise of feasibility when the mass is reduced. As a result, insights are provided on how the change in

design values affected the structural performance. The exploratory aspect of the design of experiments provides an overview about promising design values and a good initial guess for the optimization process.
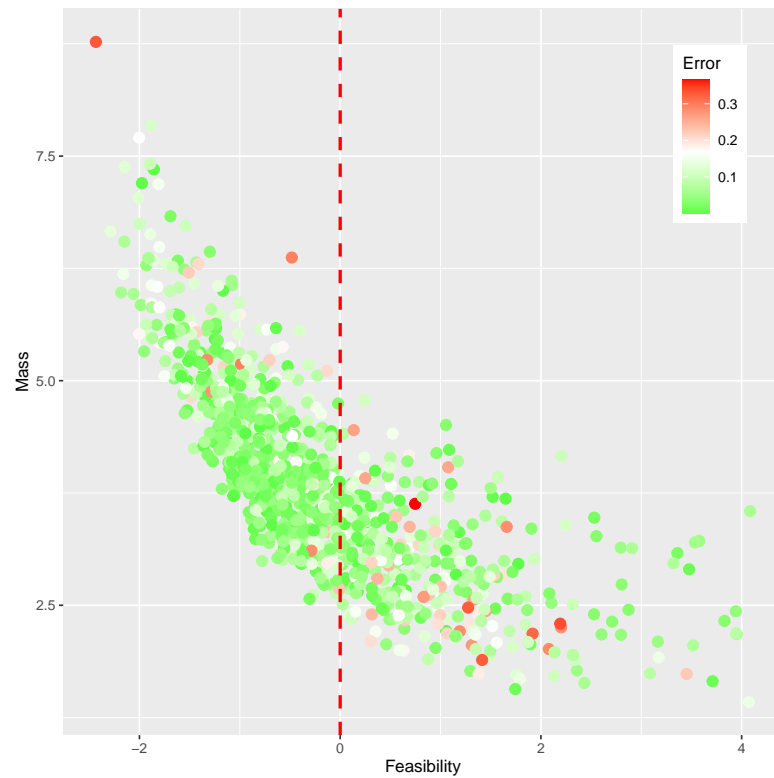

Figure 16. Mass error level $|\Delta_1|$ at several mass and feasibility values.
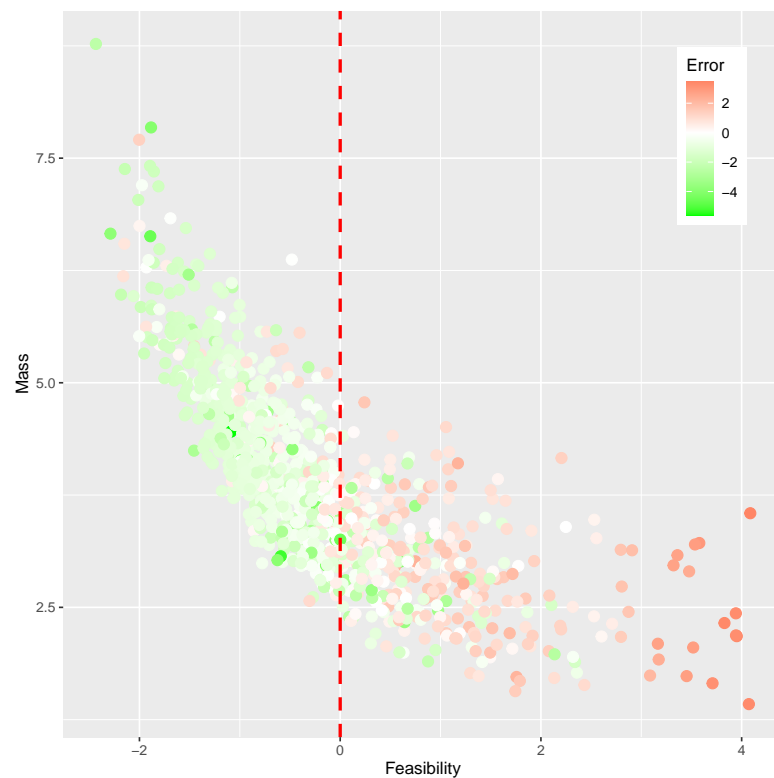

Figure 17. Feasibility error level $log(|\Delta_2|)$ at several mass and feasibility values.

4.3. Sensitivity of Parameters

Aiming to evaluate the effects of on mass and feasibility, the weighting parameter α was investigated within the range $\alpha \in [0.05, 0.95]$. Furthermore, the effects of weighting feasibility index and feasibility classifier are discussed here.

The results of the numerical optimization (Equation (24)) are now presented. Table 4 shows the initial and optimal design values, α, changed. As f_2 (Equation (20)) was evaluated by means of a regression strategy and f_3 (Equation (21)) was evaluated by a classification strategy, some discrepancies may occur when comparing f_2 and f_3 (Equation (24)). Optimal designs between lines 21 and 29 of Table 4 show $f_2(\boldsymbol{x_1}) < 1$ and $f_3(\boldsymbol{x_1}) = 1$. A contribution of the present study is the proposition of the classification index f_3 as an objective. The classification index has proven effective at identifying feasible designs. Therefore, any design is considered truly feasible if $f_2(\boldsymbol{x_1}) < 1$ and $f_3(\boldsymbol{x_1}) = 0$. Otherwise, the design is considered infeasible. The corresponding optimal designs are presented in Table 5.

Table 4. Initial and optimal objective values.

i	α	$F(x_0)$	$F(x_1)$	$f_1(x_1)$	$f_2(x_1)$	$f_3(x_1)$	Time (s)
1	0.050	2.79	0.36	2.68	0.00	0	14
2	0.075	2.88	0.52	2.63	0.00	0	15
3	0.100	2.98	0.57	2.38	0.00	0	13
4	0.125	3.07	0.80	2.52	0.00	0	12
5	0.150	3.17	0.80	2.31	0.00	0	15
6	0.175	3.26	0.99	2.38	0.00	0	12
7	0.200	3.36	1.20	2.45	0.00	0	10
8	0.225	3.45	1.41	2.51	0.00	0	11
9	0.250	3.55	1.41	2.38	0.00	0	11
10	0.275	3.64	1.38	2.24	0.00	0	11
11	0.300	3.74	1.57	2.29	0.00	0	11
12	0.325	3.83	1.70	2.28	0.00	0	12
13	0.350	3.93	1.85	2.30	0.00	0	12
14	0.375	4.02	2.05	2.34	0.00	0	15
15	0.400	4.12	2.07	2.27	0.00	0	10
16	0.425	4.21	2.21	2.28	0.00	0	10
17	0.450	4.31	2.30	2.26	0.00	0	13
18	0.475	4.41	2.52	2.30	0.00	0	10
19	0.500	4.50	2.58	2.27	0.00	0	9
20	0.525	4.60	2.70	2.27	0.00	0	10
21	0.550	4.69	2.17	1.77	0.00	1	13
22	0.575	4.79	3.04	2.30	0.00	0	11
23	0.600	4.88	2.08	1.67	0.00	1	10
24	0.625	4.98	1.47	1.28	0.17	1	9
25	0.650	5.07	1.48	1.26	0.27	1	8
26	0.675	5.17	1.48	1.24	0.37	1	10
27	0.700	5.26	1.49	1.22	0.51	1	10
28	0.725	5.36	1.48	1.19	0.67	1	10
29	0.750	5.45	1.47	1.16	0.87	1	9
30	0.775	5.55	1.46	1.12	1.11	1	9
31	0.800	5.64	1.43	1.09	1.43	1	10
32	0.825	5.74	1.39	1.04	1.84	1	9
33	0.850	5.83	1.34	0.99	2.39	1	10
34	0.875	5.93	1.27	0.93	3.16	1	9
35	0.900	6.02	1.17	0.85	4.27	1	10
36	0.925	6.12	1.04	0.74	5.99	1	9
37	0.950	6.21	0.84	0.60	8.91	1	10

The SVM-based feasibility classifier indicates an infeasible state for 16 designs. The optimization was performed using real-valued design variables. The data obtained from the metamodel optimization indicate that the mean value of 2.65 kg is a robust value for the mass index. The 37 designs shown in Table 5 were rounded to integer values to satisfy

manufacturing constraints. The integer design values were then used to compute the mass and feasibility indices with the FE model, and the results are shown in Figure 18.

Table 5. Optimal design values.

i	b	h	b_{str}	$n_{0°}^{sk}$	$n_{\pm45°}^{sk}$	$n_{90°}^{sk}$	$n_{0°}^{str}$	$n_{\pm45°}^{str}$	$n_{90°}^{str}$
1	140	40	62	1.96	6.85	1.07	8.92	2.77	2.73
2	140	40	58	1.85	7.65	1.05	9.19	1.82	2.51
3	140	40	59	1.82	7.49	1.19	9.11	1.20	1.81
4	168	40	52	2.08	8.92	1.01	8.00	2.40	2.71
5	140	40	61	2.27	6.18	1.79	8.72	1.63	2.17
6	140	40	60	2.38	7.07	1.00	8.74	1.61	1.35
7	168	40	54	2.11	8.83	1.02	7.48	2.97	1.94
8	168	40	52	1.72	9.21	1.14	7.59	2.75	1.72
9	168	40	56	2.91	7.45	1.46	8.88	2.66	1.19
10	168	40	65	1.00	6.79	1.36	8.70	1.70	2.59
11	168	42	61	1.64	4.84	5.29	8.34	1.91	2.29
12	140	40	60	2.68	4.58	3.74	9.66	1.40	1.92
13	140	41	67	1.40	3.49	6.27	9.94	1.15	1.84
14	140	43	61	1.86	5.08	3.53	8.92	1.42	2.41
15	140	40	60	1.72	4.54	5.60	9.54	1.22	1.01
16	140	40	60	1.77	4.40	6.05	9.03	1.26	1.60
17	140	40	62	1.78	4.39	5.34	8.79	2.09	1.00
18	140	40	64	2.51	3.59	6.40	8.97	1.94	1.49
19	168	40	59	2.87	3.44	7.21	8.83	2.04	1.44
20	140	41	60	2.24	4.00	5.57	9.15	2.11	1.00
21	168	44	62	2.63	4.14	4.32	8.78	1.00	1.00
22	140	40	64	2.04	5.50	2.75	8.10	1.98	1.00
23	168	42	66	1.97	5.29	2.99	7.11	1.00	1.00
24	168	45	64	1.00	7.02	1.00	1.00	1.00	1.00
25	168	45	65	1.00	6.89	1.00	1.00	1.00	1.00
26	168	45	65	1.00	6.76	1.00	1.00	1.00	1.00
27	168	45	65	1.00	6.61	1.00	1.00	1.00	1.00
28	168	45	65	1.00	6.45	1.00	1.00	1.00	1.00
29	168	45	66	1.00	6.26	1.00	1.00	1.00	1.00
30	168	45	66	1.00	6.06	1.00	1.00	1.00	1.00
31	168	46	66	1.00	5.83	1.00	1.00	1.00	1.00
32	168	46	66	1.00	5.56	1.00	1.00	1.00	1.00
33	168	46	67	1.00	5.24	1.00	1.00	1.00	1.00
34	168	47	67	1.00	4.86	1.00	1.00	1.00	1.00
35	168	47	68	1.00	4.39	1.00	1.00	1.00	1.00
36	168	48	68	1.00	3.79	1.00	1.00	1.00	1.00
37	168	50	69	1.00	2.96	1.00	1.00	1.00	1.00

The mass index deviation is presented in Figure 19. All points with mass values lower than 2.0 kg are infeasible from the structural perspective. Precise values are shown in Table 4.

As shown in Figure 20, several designs are concentrated in the range of lower $n_{90°}^{sk}$ values. Designs with lower mass index are concentrated in the area of lower $n_{\pm45°}^{str}$ and $n_{90°}^{str}$ values. Optimal feasible designs also have a trend around lower h values. Several infeasible optimal designs are grouped in the range of lower values of $n_{0°}^{sk}$ and $n_{90°}^{sk}$.

There is agreement between the optimal mass index found through the metamodeling and the values obtained by the FE model. The proposed workflow resulted in designs that are feasible and reduced the mass index. Furthermore, the optimization loop of several candidate designs gives insight into the sensitivity of the obtained solution. Distinct values of the α parameter also resulted in designs with different masses. As expected, there is a clear compromise between mass reduction and infeasibility.

To investigate the sensitivity of the proposed optimization framework to the type of DOE, a second DOE was created using a more refined discretization of the h and b_{str} design

variable levels. Next, a new metamodel was trained, followed by optimization at different α values. Figure 21 shows the optimal mass versus α parameter, with the mass computed using the FE model and the rounded-off variable values at the optimum designs obtained with the metamodel. The trade-off of mass and feasibility indices with $\alpha = 0.5$ is shown in Figure 22.
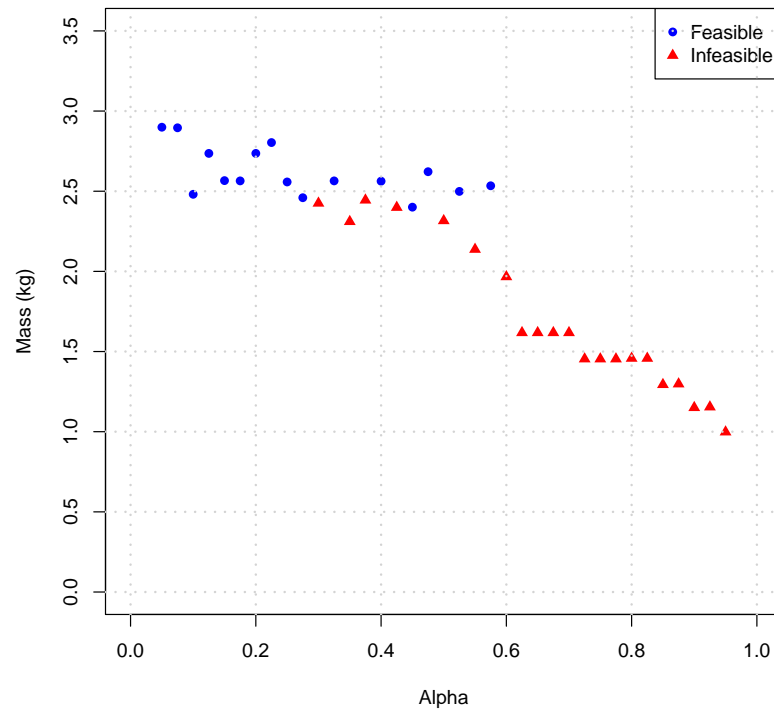

Figure 18. First DOE: optimum mass for different α values calculated by the FE model, after rounding the variables at the optimal points from the metamodel.
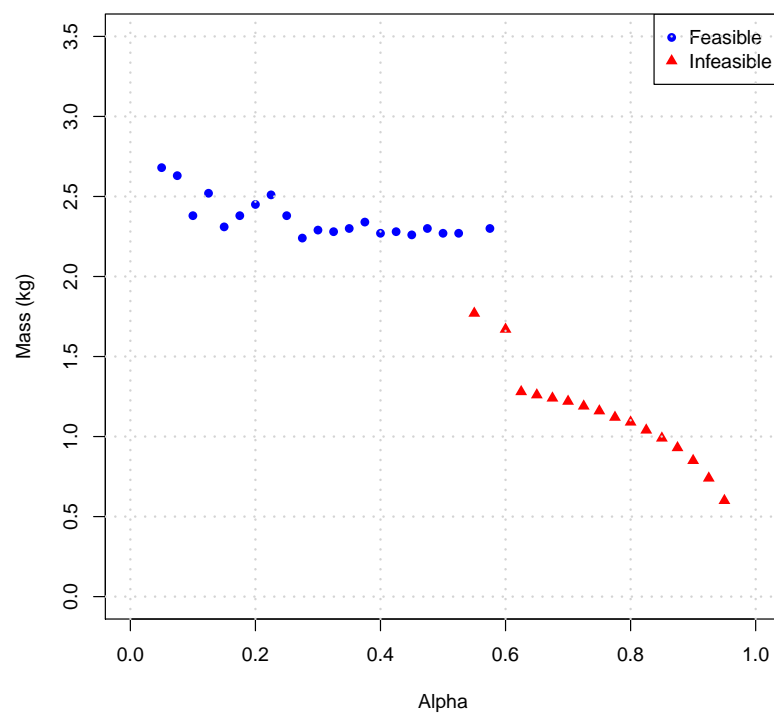

Figure 19. First DOE: optimum mass for different α values calculated by the metamodel.

The comparison of Figures 18 and 21 shows agreement of the optimal mass index in both cases. The mass and feasibility values had no significant change between the first and second DOEs, as also confirmed by the comparison of Figures 22 and 23. As the mass index decreases, the feasibility index moves towards infeasibility. As a result, the lower the probability of obtaining a given mass value, the lower the chance of achieving feasible designs.
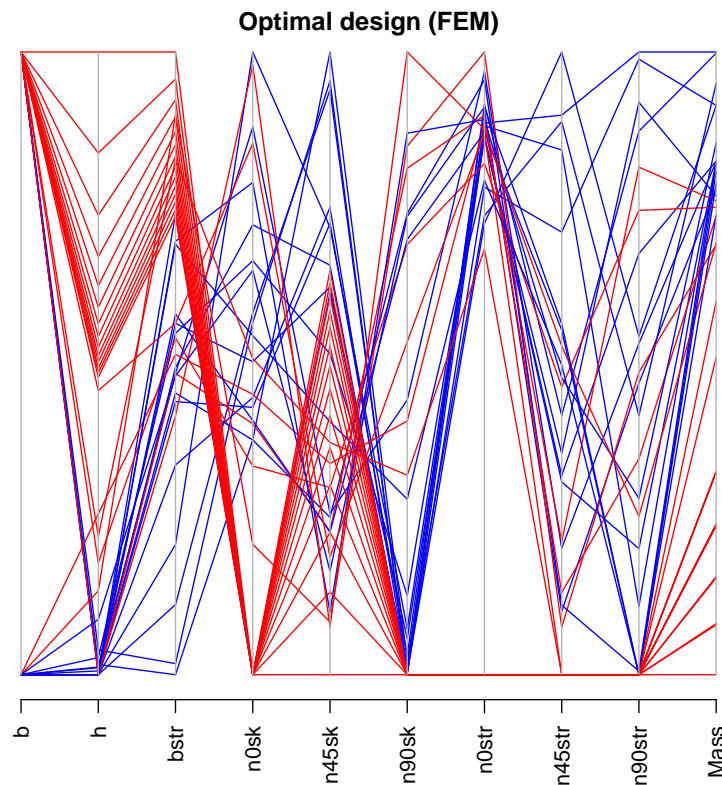
Optimal design (FEM)

Figure 20. First DOE: parallel coordinate values of optimal feasible (blue) and infeasible (red) designs.
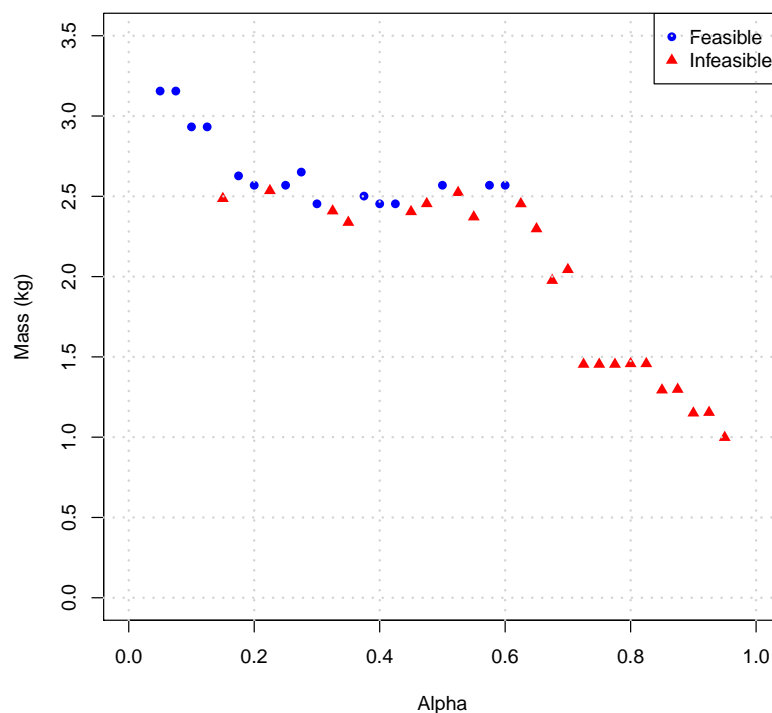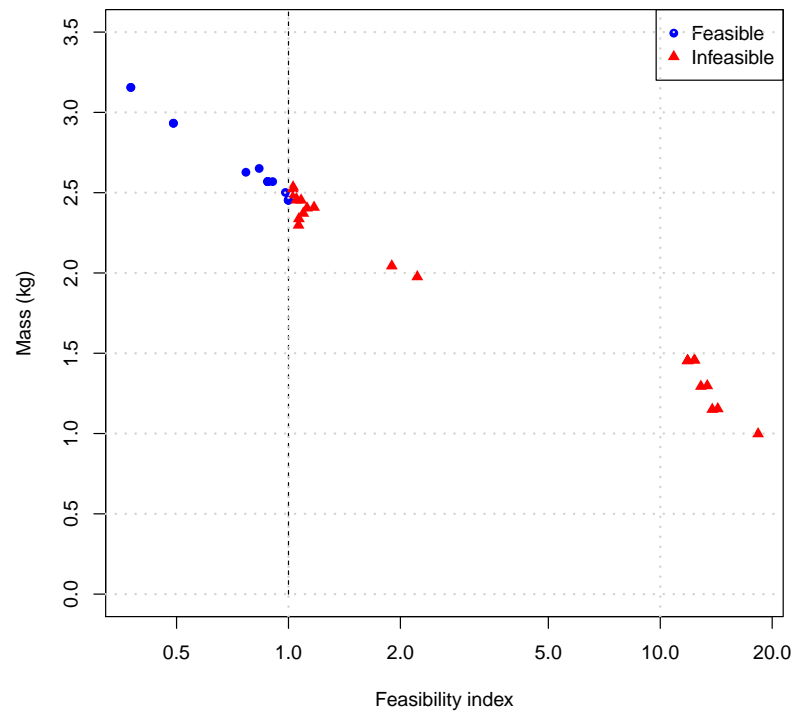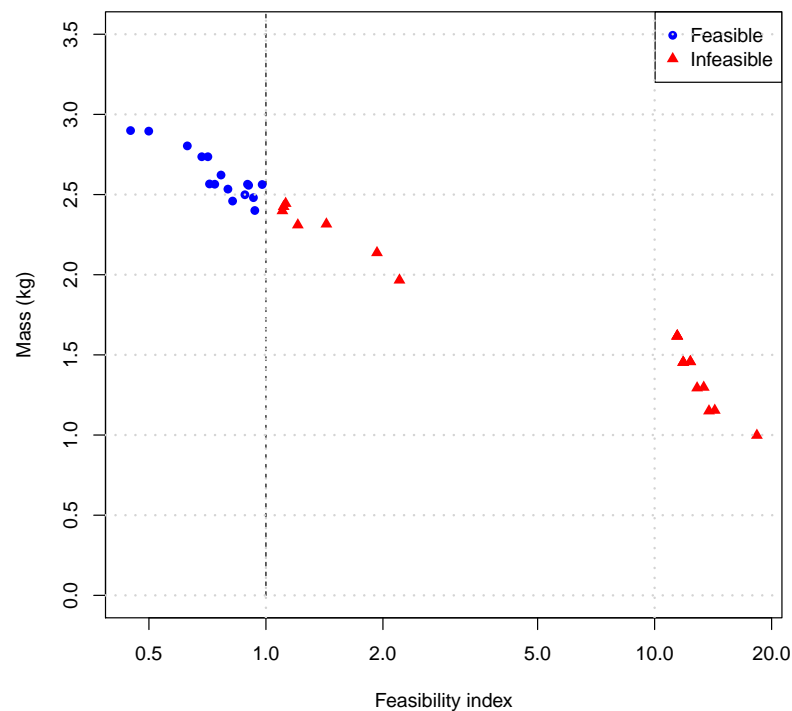

Figure 21. Second DOE: optimum mass for different α values computed by the FE model.

Figure 22. Second DOE: Pareto front of the optimum mass for different feasibility indices with $\alpha = 0.5$.

Figure 23. First DOE: Pareto front of the optimum mass for different feasibility indices with $\alpha = 0.5$.

The exploratory capabilities of the current optimization framework allow browsing amongst the feasible options. The designer can choose a target feasibility index based on minimum margins of safety, mass or other requirements. This capability is illustrated in the Pareto fronts of Figures 22 and 23. When there are no additional constraints, the feasible design that provides the minimum mass becomes a natural choice. Finally, the results of new FE evaluations can be added to the metamodel at any time to refine it in new or existing design regions.

In design problems with different numbers of variables, or for the current design problem with variables in different ranges, the new DOE is indirectly affected to handle the same errors presented here. One relevant factor to determine the necessary number of samples in the DOE is the ability of the metamodel to represent the interdependence of the design variables under investigation. More samples are required in cases where this interdependence becomes stronger, such as in structures where variable stiffness designs create a nonlinear coupling between the stiffness and geometric variables [6,21,36–40]. A comprehensive discussion about the influence of the number of design variables is provided by Myers et al. [41].

5. Conclusions

Herein was proposed a new method for optimal design of wing panels consisting of a framework that combines design of experiments, data interpolation, data classification and an optimization procedure. The methodology captures valuable information about the design space, identifying patterns and design trends discovered throughout the optimization workflow.

The exploitation of promising design regions was conducted using a deterministic optimization method. As there was no need to explicitly compute the gradient of the objective function, the method was able to navigate in a relative large area of the design space to explore the metamodel in the search for optimal alternatives.

A unique feature of the present contribution is the combination of regression and classification strategies in a multi-objective optimization formulation. Changes in the weighting parameter of the multi-objective functions proved to be an important feature for investigating the compromise between minimum mass and feasibility of the structure. Regression and classification indices in a multi-objective expression led to the effective exploration of the design space and avoided the premature convergence of the method.

The obtained Paretto fronts can be used to explicitly decide a target margin of safety for the designed panels, with a known influence on the obtained mass. In a case where no additional constraints exist and the target margin of safety is null, a natural choice for the selected design is the one with minimum mass in the entire feasible region.

Another challenging aspect of the present design problem that was well handled by the optimization framework is the simultaneous existence of discrete and continuous design variables. Usually, methods for exploring the space of integer solutions are computationally intensive and slower in convergence.

If information from new FE designs is available after the optimization cycle, the data obtained by the DOE phase can be supplemented with new information, and a new metamodeling and optimization cycle is started. It gives insights about how changes in design values influences the overall design indices.

Due to the applicability of the results found by the present analysis in the context of lightweight structures, the investigation of problems with greater complexity and more design variables is seen as the most important next step of the present research. The inclusion of design indices such as the b-factor in the initial post-buckling analyzes of imperfection-insensitive shells is also envisioned as an interesting application of the present optimization framework. There may be concurrency between designs aiming at negative b-factors and designs targeting higher linear buckling loads.

Data Availability Statement: The MSC Nastran models are generated using Python scripts. The DOE, SVM and optimizations are performed using R and C++. The respective scripts can be made available under request to Rogério R. Santos (DOE, SVM and optimization) or Saullo G. P. Castro (MSC Nastran models).

Conflicts of Interest: The authors declare no conflict of interest.

References

1. Fu, X.; Ricci, S.; Bisagni, C. Minimum-weight design for three dimensional woven composite stiffened panels using neural networks and genetic algorithms. *Compos. Struct.* **2015**, *134*, 708–715. [CrossRef]
2. Ehsani, A.; Dalir, H. Multi-objective optimization of composite angle grid plates for maximum buckling load and minimum weight using genetic algorithms and neural networks. *Compos. Struct.* **2019**, *229*, 111450. [CrossRef]
3. Ehsani, A.; Dalir, H. Multi-objective design optimization of variable ribs composite grid plates. *Struct. Multidiscip. Optim.* **2021**, *63*, 407–418. [CrossRef]
4. Thole, S.P.; Ramu, P. Design space exploration and optimization using self-organizing maps. *Struct. Multidiscip. Optim.* **2020**, *62*, 1071–1088. [CrossRef]
5. Wang, Z.; Almeida, J.H.S., Jr.; St-Pierre, L.; Wang, Z.; Castro, S.G. Reliability-based buckling optimization with an accelerated Kriging metamodel for filament-wound variable angle tow composite cylinders. *Compos. Struct.* **2020**, *254*, 112821. [CrossRef]
6. Wang, Z.; Almeida, J.H.S. Jr.; Ashok, A.; Wang, Z.; Castro, S.G.P. Lightweight design of variable-angle filament-wound cylinders combining Kriging-based metamodels with particle swarm optimization. *Preprint* **2021**. [CrossRef]
7. Chen, S.; Lin, Z.; An, H.; Huang, H.; Kong, C. Stacking sequence optimization with genetic algorithm using a two-level approximation. *Struct. Multidiscip. Optim.* **2013**, *48*, 795–805. [CrossRef]
8. An, H.; Xian, K.; Huang, H. Actuator placement optimization for adaptive trusses using a two-level multipoint approximation method. *Struct. Multidiscip. Optim.* **2016**, *53*, 29–48. [CrossRef]
9. An, H.; Chen, S.; Huang, H. Multi-objective optimization of a composite stiffened panel for hybrid design of stiffener layout and laminate stacking sequence. *Struct. Multidiscip. Optim.* **2018**, *57*, 1411–1426. [CrossRef]
10. Liu, H.; Ong, Y.S.; Cai, J. A survey of adaptive sampling for global metamodeling in support of simulation-based complex engineering design. *Struct. Multidiscip. Optim.* **2018**, *57*, 393–416. [CrossRef]
11. Awad, M.; Khanna, R. *Efficient Learning Machines*; Apress: Berkeley, CA, USA, 2015. [CrossRef]
12. Basudhar, A.; Missoum, S. A sampling-based approach for probabilistic design with random fields. *Comput. Methods Appl. Mech. Eng.* **2009**, *198*, 3647–3655. [CrossRef]
13. Missoum, S.; Ramu, P.; Haftka, R.T. A convex hull approach for the reliability-based design optimization of nonlinear transient dynamic problems. *Comput. Methods Appl. Mech. Eng.* **2007**, *196*, 2895–2906. [CrossRef]
14. Basudhar, A.; Missoum, S.; Harrison Sanchez, A. Limit state function identification using Support Vector Machines for discontinuous responses and disjoint failure domains. *Probab. Eng. Mech.* **2008**, *23*, 1–11. [CrossRef]
15. Basudhar, A.; Missoum, S. Adaptive explicit decision functions for probabilistic design and optimization using support vector machines. *Comput. Struct.* **2008**, *86*, 1904–1917. [CrossRef]
16. Basudhar, A.; Missoum, S. An improved adaptive sampling scheme for the construction of explicit boundaries. *Struct. Multidiscip. Optim.* **2010**, *42*, 517–529. [CrossRef]
17. Basudhar, A.; Dribusch, C.; Lacaze, S.; Missoum, S. Constrained efficient global optimization with support vector machines. *Struct. Multidiscip. Optim.* **2012**, *46*, 201–221. [CrossRef]
18. Song, H.; Choi, K.K.; Lee, I.; Zhao, L.; Lamb, D. Adaptive virtual support vector machine for reliability analysis of high-dimensional problems. *Struct. Multidiscip. Optim.* **2013**, *47*, 479–491. [CrossRef]
19. Carnell, R. lhs: Latin Hypercube Samples R Package, Version 1.0.2. 2020. https://CRAN.R-project.org/package=lhs (accessed on 20 October 2021).
20. Fenner, P. Comparing the Accuracy of VICONOPT to FEM for Analysing Aircraft Wing Skin Type Panels. Master's Thesis, Loughborough University, Loughborough, UK, 2014.
21. Machado, T.G.; Hernandes, J.A.; Capacia, V.; Castro, S.G. Design of Compressed Variable Stiffness Panels with Steering-thickness Coupling. In *AIAA Scitech 2021 Forum*; American Institute of Aeronautics and Astronautics: Reston, Virginia, 2021. [CrossRef]
22. MSC. *MSC Nastran Quick Reference Guide*; MSC Software: Newport Beach, CA, USA, 2017.
23. Kassapoglou, C. *Design and Analysis of Composite Structures*; John Wiley & Sons Ltd.: Oxford, UK, 2013. [CrossRef]
24. Megson, T.H.G. *Aircraft Structures for Engineering Students*, 4th ed.; Butterworth-Heinemann: Kidlington, UK, 2007; p. 1179.
25. Niu, C. *Airframe Structural Design: Practical Design Information and Data on Aircraft Structures*; Conmilit Press Ltd.: HongKong, China, 1988; p. 612.
26. Reddy, J.N. *Mechanics of Laminated Composite Plates and Shells*; CRC Press: Boca Raton, FL, USA, 2003. [CrossRef]
27. Russell, S.; Norvig, P. *Artificial Intelligence A Modern Approach*, 3rd ed.; Prentice Hall: Broadway, NC, USA, 2010.
28. Salcedo-Sanz, S.; Rojo-Álvarez, J.L.; Martínez-Ramón, M.; Camps-Valls, G. Support vector machines in engineering: An overview. *Wiley Interdisc. Rev. Data Min. Knowl. Discov.* **2014**, *4*, 234–267. [CrossRef]
29. Steinwart, I.; Thomann, P. LiquidSVM: A fast and versatile SVM package. *arXiv* **2017**, arXiv:1702.06899.

30. Rosenblatt, F. The perceptron: A probabilistic model for information storage and organization in the brain. *Psychol. Rev.* **1958**, *65*, 386. [CrossRef]

31. Poggio, T.; Girosi, F. *A Theory of Networks for Approximation and Learning*; Technical Report; Massachusetts INST of TECH Cambridge Artificial Intelligence LAB: Cambridge, MA, USA, 1989.

32. Bergmeir, C.; Benítez, J.M. Neural Networks in R Using the Stuttgart Neural Network Simulator: RSNNS. *J. Stat. Softw.* **2012**, *46*, 1–26. [CrossRef]

33. R Core Team. *R: A Language and Environment for Statistical Computing*; R Foundation for Statistical Computing: Vienna, Austria, 2020.

34. Powell, M.J.D. *The BOBYQA Algorithm for Bound Constrained Optimization without Derivatives*; Cambridge NA Report NA2009/06; University of Cambridge: Cambridge, UK, 2009.

35. Johnson, S.G. The NLopt Nonlinear-Optimization Package, 2020. Available online: https://github.com/stevengj/nlopt (accessed on 20 October 2021).

36. Blom, A.W.; Abdalla, M.M.; Gürdal, Z. Optimization of course locations in fiber-placed panels for general fiber angle distributions. *Compos. Sci. Technol.* **2010**, *70*, 564–570. [CrossRef]

37. Kim, B.C.; Potter, K.; Weaver, P.M. Continuous tow shearing for manufacturing variable angle tow composites. *Compos. Part A Appl. Sci. Manuf.* **2012**, *43*, 1347–1356. [CrossRef]

38. Castro, S.G.; Donadon, M.V.; Guimarães, T.A. ES-PIM applied to buckling of variable angle tow laminates. *Compos. Struct.* **2019**, *209*, 67–78. [CrossRef]

39. Vertonghen, L.; Castro, S.G. Modelling of fibre steered plates with coupled thickness variation from overlapping continuous tows. *Compos. Struct.* **2021**, *268*, 113933. [CrossRef]

40. Ummels, R.; Castro, S.G. Overlap-stiffened panels for optimized buckling performance under minimum steering radius constraints. *Compos. Part Open Access* **2021**, *6*, 100174. [CrossRef]

41. Myers, R.H.; Montgomery, D.C.; Anderson-Cook, C.M. *Response Surface Methodology: Process and Product Optimization Using Designed Experiments*; John Wiley & Sons: Hoboken, NJ, USA, 2016.